IAC-23-A6.1.4.79175

Laser Ranging to Space Debris: Overcoming Challenges

Julian Rodriguez-Villamizar[a]*, Thomas Schildknecht[a]

[a] *Astronomical Institute, University of Bern, Sidlerstrasse 5, CH-3012 Bern, Switzerland,* julian.rodriguez@unibe.ch
* Corresponding Author

Abstract

Space debris laser ranging systems are a valuable asset complementing existing observation technology for space surveillance, space situational awareness and space traffic management. The technique is promising for orbit determination and improvement if compared to radar observing systems due to its achievable precision, and the advantageous capability to operate in the absence of an external illumination source irradiating the target object as needed when utilizing passive-optical systems. Additionally, an extended set of observables per target object may be extracted from the acquired laser ranges comprising information such as horizontal angular observations from the pointing direction, the tumbling motion, the average cross-section, or the surface albedo of the observed target object.

For the successful employment of laser ranging systems in space surveillance and tracking applications, it is required that the systems are equipped with: a) a target acquisition and beam locking subsystem to compensate for inaccurate ephemerides and the relatively narrow field of view of the laser beam; b) high output power, which is a critical specification when ranging to targets that do not carry any reflective element on board; c) selected band-pass and temporal filters to potentially enable the acquisition of observations during daylight. Recent work conducted in this area has shown feasible solutions addressing the previous constraints. Nevertheless, while finding new solutions to the aforementioned tasks, we found new challenges. In the scope of this presentation, we will focus on the detection of the weak signal resulting from the system specifications, the type and physical characteristics of the irradiated target object, its attitude state, and the impact of the available ephemerides. Note that the previous factors become noticeable in the signal signature, which can be seen in the so-called residuals: actual observations minus predictions. In this context, we will revisit existing algorithms for signal detection currently in use by many traditional geodetic Satellite Laser Ranging stations, and formulate the problem from a hypothesis testing perspective from which we will present encouraging preliminary results.

Keywords: Laser Ranging, Signal Detection, Space Debris target objects.

Acronyms/Abbreviations

SLR	- Satellite Laser Ranging
ToF	- Time of Flight
SPAD	- Single-photon Avalanche Diode
SSA	- Space Situational Awareness
ROC	- Receiver Operating Characteristic

1. Introduction

Laser ranging to space debris is arguably an attractive observation technique for space situational awareness applications, among others. The reasons are the precision of the measurement technique, with an equivalent mm accuracy after a proper calibration of the system, the active operating mode, and the information content that we can extract from the observable itself. However, to exploit the full potential of the technique in the domain of SSA and neighbouring fields, there are some technical requirements that have to be accounted for being able to collect usable observations. Within those technical challenges, we find the average power of the laser as a function of emitted energy per pulse and the repetition rate of the station. Traditional systems work with low energy and relatively high repetition rates. This combination yields on average 1 W for many of the so-called geodetic Satellite Laser Ranging stations. The low power is compensated by the space segment, which includes retroreflectors on board of certain missions for which precise orbit determination of the spacecraft was foreseen. Those missions, which in addition might have a controllable attitude while the mission is active, are known as cooperative targets. Bearing this in mind, to extend the technique to SSA applications, we have to consider that, in principle, the targets of interest will not be equipped with retroreflectors i.e., non-cooperative targets, thus weakening the link budget for the geodetic type of laser systems. Furthermore, the fact that there are not publicly available precise ephemerides will pose a twofold challenge. Firstly, we will need an aiding system to help focusing the laser beam on the target, since the field-of-view of the laser beam might be of about 20 arcseconds. Secondly, we will need to extend the listening windows for the returns, i.e., the range gates, which is a

multiplicative factor for the noise photons that might trigger an event in the detector, which poses a difficulty for pinpointing the actual events that were triggered by the photons reflected by the target. Note that if the attitude of the object is uncontrolled, the difficulty of the challenge may increase.

Finally, if we consider the usability of the technique for SSA and similar applications, there is the need to maximize the observation windows. The latter may be achieved by enabling daylight observations. To carry out laser ranging observations during daylight, additional hardware and software requirements to those commonly used by SLR stations become imperative [1].

Example of daylight observations to space debris may be found in [1, 2, 3, 4]. The previous references show successful technical solutions enabling the acquisition of range measurements to non-cooperative space debris targets with heterogeneous systems. Nevertheless, despite the technical challenges posed to get identifiable *valid* returns from the target object, there are still some challenges to be solved. For example, how can we reliably extract the signal when the signal-to-noise ratio is compromised? On the same note, how can we compensate for the signature of the residuals - being defined as the actual observations minus the predictions at the same epoch using the available tracking ephemerides? As we will see, there might be situations depicting a noticeable steep signature, which will pose a challenge to traditional bivariate histogram binning approaches. In the current work, we address those two specific questions. In the following, we will provide more insight into our assumptions, which will be validated by comparing simulated measurements against real ones. Once we present the software tool that generates the synthetic observations, we will present the so-called Receiver Operating Characteristic curves. ROC curves are a suitable method to find optimization parameters such as the threshold for noise photons, bin size in observation time and the bin size fitting best to the target depth, and even the shape of the bin used to construct the bivariate histograms.

1.1 Statistical Observation Model

The work presented in this paper will be based in known theoretical probability distributions. To ensure realism between the theory and observations, we analyse a series of observations collected by the laser system at the SwissOGS to an external calibration target located 600 m apart from the reference point of the telescope during one minute. The observations are the round trip time-of-flight of a laser pulse plus noise and are shown in Fig.1. Likewise, we present the temporal distribution of the collected observations in the upper histogram, binning the data every 0.30 seconds. The average return

rate using this binning yielded 23 detections/bin. Note that in this phase we are not distinguishing between noise and signal. In addition, the right histogram depicts the spatial distribution of the observations along the so-called range gate. The range gate is a temporal window, which is centred at the expected return epoch of the emitted pulse after being reflected by the target object. The width of this gate depends on the certainty that we have on the expected return epoch of an emitted laser pulse. Finally, the right histogram in Fig.1., with a bin-width of 125 nanoseconds, shows clearly the distribution of the noise and that of the signal for which its bin exceeds the 500 counts.
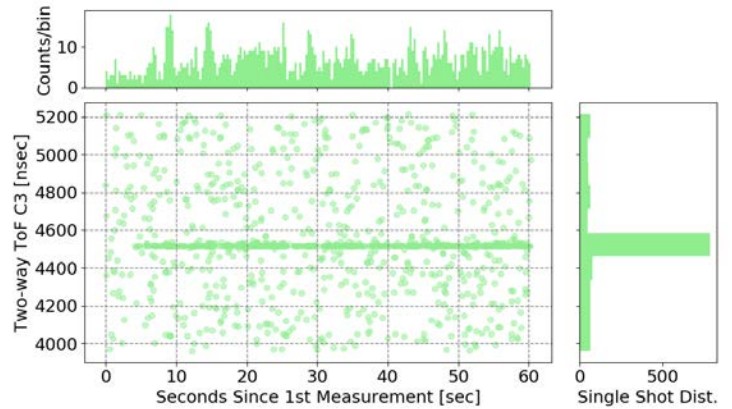
Fig. 1. Measurements taken by the laser ranging system at the SwissOGS to an external calibration target. The histograms show the temporal distribution of the observations epoch wise and along the so-called range gate.

In the following, the detection of photons may be seen with two different statistical approaches. The first one will model the behaviour of the system in terms of photon rates, while the second one might be parametrized in terms of trials such as, out of a given number of pulses, how many of those did successfully trigger a signal event after reflection by the target object? The first approach may be described with a Poisson distribution with a unique parameter i.e., the stationary rate of the event itself. The second approach will need to define the number of trials together with prior knowledge about the probability of success. In the following, we will consider the first approach only, since the parametrization of the problem is simplified without losing any physical information of the problem that we want to tackle.

Once we know that our statistical model will be described by the Poisson probability distribution, we define the types of rates that we will have. On the one hand, we have the signal, which is the successful photons coming back after reflection by the target object to the detector as a function of the parameters given by the optical link. On the other hand, we consider as noise

events those photons that trigger a detection event on the detector due to background or dark current. Bearing this in mind, and making use of the additive property of the Poisson distributions, we are expecting such distribution being parametrized with a unique rate corresponding to the sum of all rates.

In Table 1, we compare the number of return rates that are drawn from the observed distribution of events at the detector with the ones extracted from a theoretical Poisson distribution. For this comparison, we construct new bins (60) for the return rates drawn from the observations and from the theoretical distribution.

Table 1. Comparison between the events observed in a sample extracted from actual observations (see Fig.1) against a theoretical Poisson distribution.

Counts/bin	OBS	THE
0	42	41
1	2	2
2	2	2
3	2	2
4	1	3
5	2	4
6	0	2
7	0	0
8	0	0
9	0	1
10	0	1
11	1	0
12	0	1
13	0	1
14	0	0
15	0	0
16	1	0
17	1	0
18	1	0
19	1	0
20	1	0
21	0	0
22	0	0
23	1	0
24	1	0
25	0	0
26	1	0
Sum	60	60

Both observations and theoretical values seem in agreement after the number of counts per bin exceed the number 16 (verified also using a chi-squared goodness of fit test). This may be explained by the behaviour of the detector, which might be attributed to *after pulsing* effects. This effect may pollute the theoretical distribution by adding tails corresponding to counts that are not spread according to a Poisson distribution. Nevertheless, this effect does not pose a serious risk for

the detection process itself, while it has to be taken care to ensure the removal of systematic effects on the observable itself.

2. Experimental setup

Once we have analysed the statistical method that will characterize the distribution of our observations, and compared it against real observations, we proceed with the simulation of scenarios that will be as close as possible to the ones encountered during regular observations. To do so, we developed a simulator. In Fig. 2. We show a generic schematic explaining the workflow of the software tool.
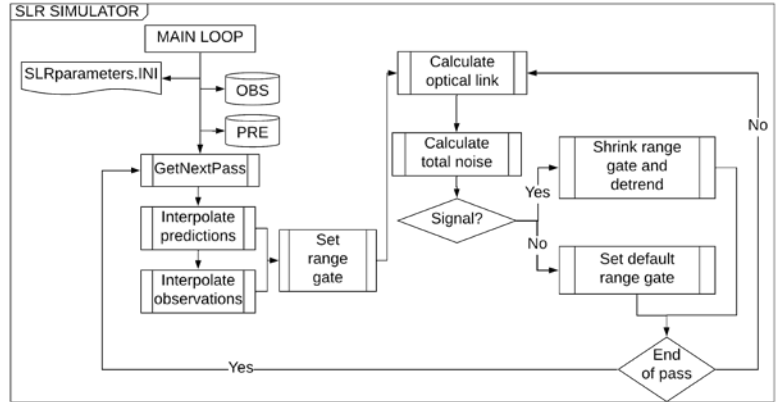
Fig. 2. Schematic of the developed simulation tool for testing different strategies for the correct discrimination of the backscattered photons from the target object from the total noise.

The simulator needs an initialization file together with two types of ephemerides with presumably different quality. There is one from which we will extract the actual observations (OBS), thus implicitly of higher accuracy, if compared with the ones, which will simulate the tracking ephemerides (PRE). The initialization file contains all system specific information that will be needed further on to compute the optical link and the total noise per trial. Once an observation pass is available for the defined observation station, we generate a number of data entries for that pass using the repetition rate of the station. Likewise, per each pass we retrieve angular and range information, together with information about the elevation of the Sun to construct the so-called noise model. Per each entry, the width of the range gate is defined, but a default value is available in the INI file. Once we have the rates for the noise and for the signal, we can generate both type of events on the receiver for a classification step. In the classification step, we added an ad hoc feature that includes the adaptability of the range gate width, if the signal is correctly discriminated from the noise. Now

the question is how are we actually discriminating between these two classes?

3. Theory and calculation

In this section, we provide a general insight into the problem of detecting the signal of interest in an optimal fashion. To do that, we examine in closer detail the models that we have for both classes: the signal and the noise.

3.1 The detector type

The type of operating mode for the detector corresponds to a single-photon avalanche diode (SPAD). We may trigger an avalanche of photoelectrons after the reception of a photon coming from the target, the background or triggered due to thermal release of energy in the detector. It could also be that there is no signal for a given trial; therefore, we have no detection event for that particular entry. The latter will occur only when the number of photons coming from either the signal or the noise is smaller than one. In addition, the detector itself cannot distinguish between the type of photon that triggered an event, therefore we have to set up a random process model in which both outcomes are equally likely. The latter was implemented in the form of samples drawn from a uniform distribution. In a subsequent step, we construct Poisson distributions using the expected photon rates from the optical link and for the calculation of the total noise. From those distributions, samples are drawn and the following cases are evaluated:

a) **No event** occurred due to a minimum number of photons from the signal and from the noise, being less than one.

b) **Noise** for those cases where the random event at the detector level will be triggered by a noise event and the sample extracted from the distribution of the noise is greater than one.

c) **Signal** for those cases where the random event at the detector level will be triggered by a signal event *and* the probability of the number of samples belonging to the distribution of the signal is greater than the probability of the samples drawn for the noise belonging to the distribution of the noise. As before, the sample for this event has to be greater than 1.

Next, we will define how we get the rates for both the signal and the noise.

3.2 Noise

We refer to noise as those photons that triggered an event in the detector, without being reflected by the target object. Specifically, we consider the diffusely scattered solar photons and the dark counts. Note that the solar photons are only accounted for when the pass of the target of interest occurs during daylight. The number of diffusely scattered solar photons is extracted using LOWTRAN. By default, we assume an angular distance of 45° between the target object and the Sun, an elevation of 1000 m and a multiple-scattering radiative transfer process. A reference value for the defined on ground solar spectral radiance is 0.0095 W/m2 str Angs. For the dark counts, we take by default the value of 400 kHz, but reference values for different system configurations are available in [5]. Having these important parameters, we can estimate the mean rate for what we will refer to as noise. The next step is critical since we have to model the distribution of such events over time and over the range gate. In an ideal scenario, the noise photons may be distributed uniformly along the range gate and in time (see e.g., the right histogram in Fig. 1.). However, in several experiments we noticed that when we removed the Fabry-Pérot filter, we had a distribution, which resembled more the sum of two exponential distributions rather than a uniform one. Two models were implemented in the simulation tool, and will be enhanced in future steps. In Fig. 3, we show an example of one of the available models, in which the noise is modelled as uniformly distributed along time and along the range gate considering only the dark counts i.e., a night-time pass. In the same figure, we compare the modelled noise against actual observations.
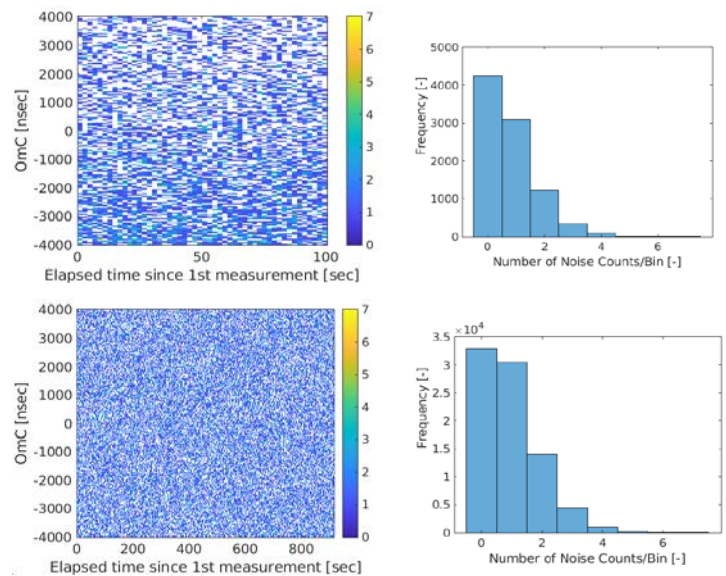
Fig. 3. The upper left-plot depicts night noise observations acquired with the available laser system at the SwissOGS. The left plots show the bivariate histograms associated to a binning of 1 second in time

(x-axis), and 20 nanoseconds along the range gate (y-axis). Likewise, the histograms on the right provide the distribution of the counts, respectively.

We see that in terms of counts and spatial distribution along the range gate, the model is consistent with the values that we usually observe in our system. Note that even though the density of the bottom plot seems to have a higher density, the effect is only due to a larger observation window (900 s) than the one we used for the observations (100 s). The same effect explains the large number of counts for the bottom histogram compared to the upper one. An additional cross-check included the comparison of statistical descriptors, which showed a remarkable resemblance for both the model and the observations. To account for a more complex behaviour, and motivated by the fact that we saw a different noise distribution after modifying the hardware setup, we implemented a skewed Gaussian distribution of the noise along the range-gate. The observations (upper plot) as well as the modelled ones (bottom plot) are shown in Fig. 4.
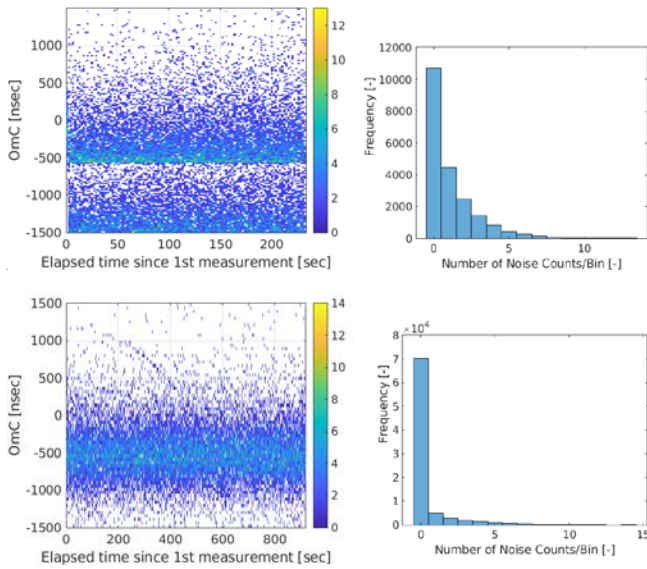
Fig 4. The left-upper plot depicts night noise observations acquired with the available laser system at the SwissOGS after removing the Fabry-Pérot filter from the receiving chain. Both left plots show the bivariate histograms associated to a binning of 1 second in time (x-axis), and 20 nanoseconds along the range gate (y-axis). Likewise, the histograms on the right provide the distribution of the counts, respectively.

This model will need to be enhanced, since a Gaussian distribution does not seem to match the distribution of the observations. In an attempt to explain the behaviour of the observations, we could argue that it might be given by the presence of stray light, since we have a

monostatic system sharing emitting and receiving chains. This effect is mitigated by the Fabry-Pérot, which spectrally filters only the radiation that is coming normal to the position of the filter, while in the absence of this filter the stray light might come from any possible direction.

3.3 Signal

For the generation of the signal, we need a reference trajectory (PRE) together with the one from which we will extract the observations (OBS). In the following examples, we will only consider an AJISAI-like orbit, corresponding to a low Earth orbiter, near circular orbit with an inclination of about 50°. The technical specifications for this case study are taken from the system available at the SwissOGS. The reader should refer to [1] for a more detailed description of the different technical components. From the simulated observations we extract the slant range, horizontal angular observations, and together with the technical specifications of the stations, we are able to derive number of photons per shot after the calculation of the optical link equation. The total number of shots are provided by the repetition rate of the station, and optionally, there is the possibility to select a given elevation mask. Finally, the model that we implemented, for the complete system response, assumes that the resulting distribution of the signal is Gaussian. Hence, the system response will be characterized by the mean, at exactly the OmC value per shot, together with the standard deviation, which will capture the target depth.

As previously done, we compare now observations coming from the system at the SwissOGS to the target object Ajisai and compare the observations against modelled values.
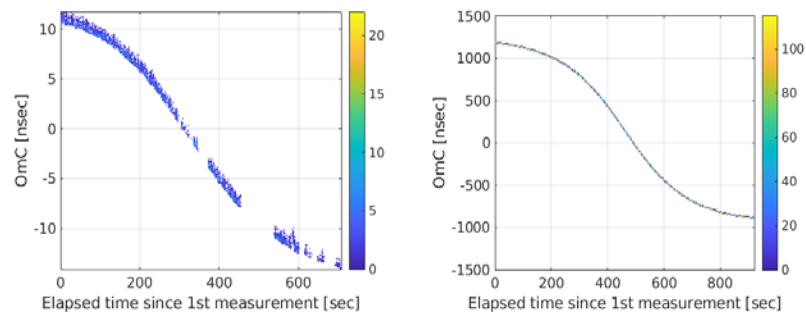
Fig. 5. Left: bivariate histogram with 1 second binning on the x-axis, and 20 nanosecond on the y-axis for real observations to Ajisai. Right: bivariate histogram with same dimensions as for the left one for the simulated observations.

The number of counts gives the first striking feature. The real observations are controlled according to a pre-defined return rate of 10 %, which explains why on average we have mostly bins with 10 detections per 1
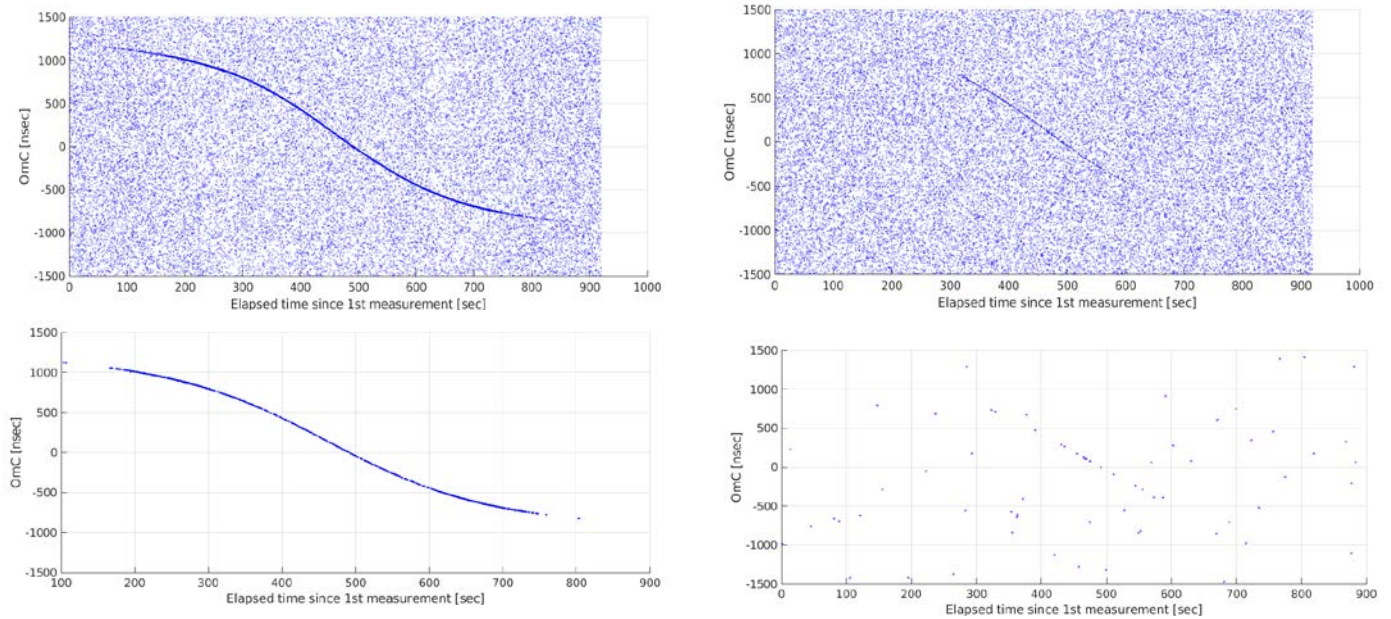
Fig. 6. The left upper plot shows the simulated data using the estimated optical cross-section for Ajisai. On the right plot, we decrease the optical cross-section until reaching the minimum signal, which is, however, enough to trigger some events close to the culmination of the target object. Both bottom plots show the screened returns using a generic configuration consisting of a threshold of 6 photons for the left and of 4 photons to the right for bins of 2 seconds along the x-axis and 1 nanosecond along de y-axis. It is also important to consider that the target depth of the object was set to 1 nanosecond.

second bin in the x-axis and 20 nanosecond bin in the y-axis. Secondly, the behaviour of the signal seems to be skewed to the left, which might correspond to the effect of after pulsing, which was addressed before. That implies that an improvement of the system response needs to be conducted in a follow-up work. Finally, if we compare the range of values for the OmC, we immediately recognize that the tracking ephemerides for the real observations were in fact of high quality compared to the ones used for our simulation. The latter were selected with a worse quality on purpose to assess the applicability of the discriminating process for space debris targets.

3.4 Observations

Once we have described our statistical model, the noise and the signal, we proceed with the simulation of observations. The station used for the simulation is the SwissOGS including its technical specifications for the laser system. In Fig. 6, we show the resulting raw observations that are the outcome of our simulation tool. In the following, we compare two scenarios that will highlight the need of optimizing certain parameters for the correct classification of events that correspond to the signal of interest. In the upper-left plot in Fig. 6, we see a common observational result for a cooperative target. The clear trace of the returns is evident even before classifying the different entries. The corresponding left-bottom plot shows the events that were classified as

signal. At first glance, it gives the impression that the algorithm is performing well. To simulate a scenario where the signal-to-noise ratio is compromised, we use as leverage the optical cross-section. Once we decrease the optical cross-section until reaching a significant weak signal at the time of closest approach, we conduct an analysis of the length of the discernible signal trace together with the subsequent classification of the weak returns. On the right-upper plot in Fig. 6, we see how the length of the discernible trace is reduced when compared to the one with the original cross-section of the target. However, regardless of the shorter discernible trace, it can be distinguished by the naked eye. One might even expect a successful detection as in the first case. In a second step analysis, we proceed with the filtering of the original raw data to extract the signal. The results after the classification step are shown in the bottom-right plot in Fig. 6. There we have the evidence that the classification procedure is not performing as optimal as in the other case. The latter gives the perfect motivation for a quantitative analysis of the classification step.

3. Results

Once we are able to simulate the observations, the remaining task is to assess quantitatively the impact of the different factors that play a role in the classification step. We distinguish clearly the impact of the threshold

of number of photons per bin, the dimension of the bin and the shape of the bin. To assess the goodness of the classification, we will use the so-called Receiver Operating Characteristic (ROC) curves, which show the performance of a detector in terms of correctly classified events as signal against those events that were classified as signal even though are noise. The latter are referred to as false alarm detections. In the previous section, we assessed the performance of the classification in a qualitative fashion i.e., we inspected visually the filtered plots to assess subjectively how good the classification was. In Fig. 7, we show the performance of the classification quantitatively by using the ROC curves.
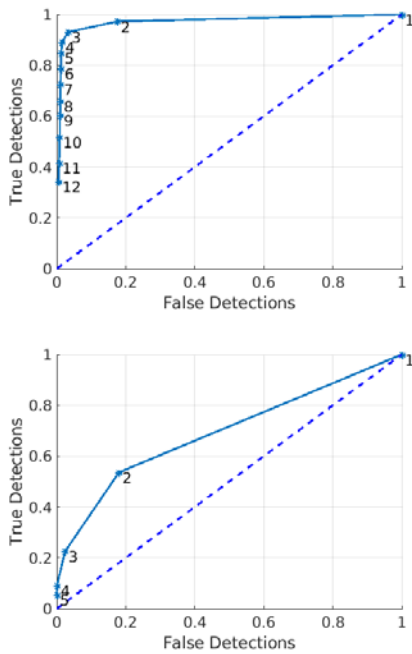
Fig. 7. Receiver Operating Characteristic curves for the synthetic data generated and depicted in Fig. 6. The upper plot corresponds to the result for the upper-left plot in Fig. 6, while the bottom one corresponds to the upper-right plot in Fig. 6. The numbers associated to each data point in both plots correspond to the threshold set for that particular solution.

The upper plot in Fig. 7, corresponds to the case study where the cross-section of the target object corresponds to the estimated one (in the order of 10^6 m2). The ROC curve shows that in this case our receiver is performing close to an ideal receiver, which is defined as a receiver that only classifies entries as signal, without any exception. On the other hand, as soon as the curve tends to the diagonal of the plot, the receiver is showing that both detections of signal or noise are

equally likely. For our first case with the original cross-section, we have a performance close to ideal as soon as we fix the threshold to a value of 3, which in turn is a value that appears repetitively in the literature for the minimization of false detections. In other systems, there is a trend to overshoot the solution, since thresholds of 10 photons/bin are selected and there is arguably a loss of good entries, which could be prevented.

Contrary to the encouraging performance of the receiver for the high signal-to-noise scenario, we see that when the average signal decreases, the behaviour of the detector worsens. It is to be expected, since the distribution of the returns coming after reflection by the target object and the distribution of the noise almost overlap making it equally likely that the events could be either signal or noise. Now, we can formulate the problem as of a multivariable optimization one. Specifically, we want to find the best combination of bin shape, size and threshold that minimizes the probability of false detections and maximizes the probability of the true detections.

To tackle this problem, we present in the following an iterative approach where we start analysing changes in the input variables and their respective impact on the ROC curves. We will only focus on the challenging case, which corresponds to the one of the weak signal-to-noise ratio, but the analysis may be easily extended to any other scenario or system. Likewise, we present preliminary results, since there are important improvements to do in the modelling of some modules of the tool.

Optimization of bin length in the x-axis

Firstly, we will assume a rectangular shape for the bin and a variable length as a function of time in the x-axis. In Fig. 8, we show the impact of a varying bin length in the ROC curves.
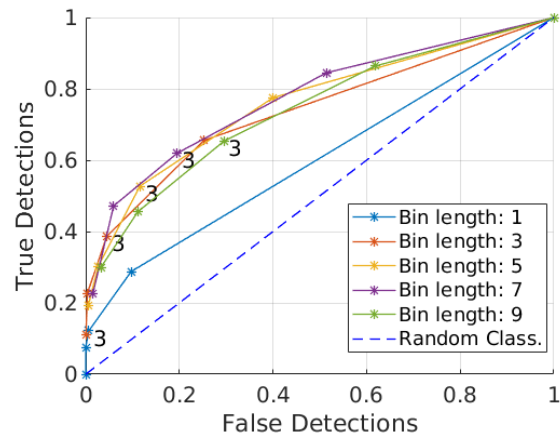
Fig. 8. Receiver Operating Characteristic curves for the classification problem varying the length of the bin size in the x-axis. Units of the bin length in seconds.

From Fig. 8, we can see how with a bin length of 5 seconds, we can have a higher true detection probability than if we used a bin size of 2 seconds as used for the plot in Fig.7. We can also see that as soon as we increase the length too much, we start increasing severely the number of false positives, which is a suboptimal behaviour of the classification process.

Optimization of the bin length in the y-axis

This part is critical as well since it is heavily correlated with the bin length on the x-axis. So each of our solutions should consider also a variation of the bin length in the x-axis. This behaviour was relatively easy to quantify, since for small values of the bin length in the x-axis, the ROC curves, as a function of the bin length in the y-axis, were barely changing, and when it was too large, was worsening quickly. In the next plot, we show examples for the optimization of the bin length in the y-axis fixing the bin length of the x-axis to 5 seconds.
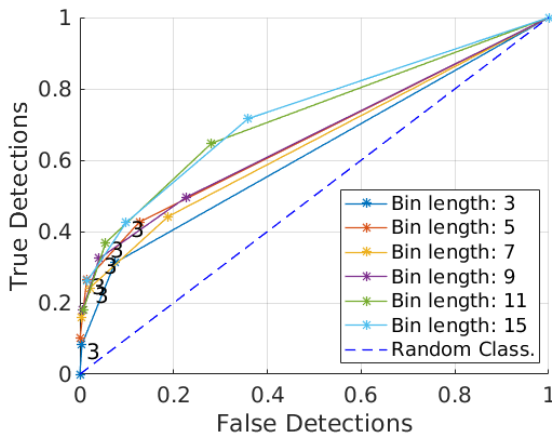
Fig. 9. Receiver Operating Characteristic curves for the classification problem varying the length of the bin size in the y-axis after fixing the bin size in the x-axis to an optimal value of 5 seconds. Units of the bin length in nanoseconds.

From Fig. 9, we can see how a larger bin length improves the probability of detection, while keeping it short decreases the performance of the classification procedure. Up to now, the parameters that yield the best solutions for a rectangular shape are 5 seconds for the length of the bin in the x-axis and 20 nanoseconds for the length of the bin in the y-axis. The remaining parameter that will be optimized is the bin shape. So far, only rectangular grids are used for the construction of

the bivariate histograms. Here, we propose a novel geometrical construction based on regular polygons. In the following, we present a new representation of bins based on hexagons, which initially are constructed based on an initial grid, which uses our optimized values for the bin length in the x- and y-axis, respectively.

Optimization of the bin shape

Regularly shaped grids can only be comprised of equilateral triangles, squares, or hexagons, as these three polygon shapes are the only three that can tessellate (repeating the same shape over and over again, edge to edge, to cover an area without gaps or overlaps) to create an evenly spaced grid. Hexagons reduce sampling bias due to edge effects of the grid shape, being explained by the low perimeter-to-area ratio of the shape of the hexagon. As an example, a circle yields the lowest ratio, but cannot tessellate to form a continuous grid. Hexagons are the most circular-shaped polygon that can tessellate to form an evenly spaced grid. This circularity of a hexagon grid allows it to represent curves in the patterns of the data more *naturally* than rectangular grids, which in this context is a desired feature, since we know that the trace of the signal returns has such trends clearly depicted in the OmC vs. time plots. In Fig. 10, we show the results of the ROCs, after changing the length of the bin size in the y-axis, fixing the one in the x-axis to 5 i.e., as in the previous figure, but this time using hexagons instead of rectangles for the bin shape.
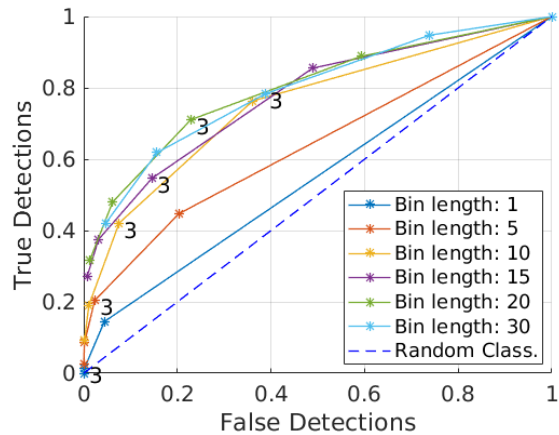
Fig. 10. Receiver Operating Characteristic curves for the classification problem varying the length of the bin size in the y-axis after fixing the bin size in the x-axis to 5 seconds. The shape used for binning this data is a hexagon grid. Units of the bin length in nanoseconds.

The results suggest an improvement on the detector performance classification once we have larger values of the length on the bin in the y-axis. The shape of the curves as soon as the length of the bin in the y-axis increases tends to move to the optimal corner of the ideal detector. There is, however, a non-negligible probability for the false alarm entries, which suggest that a post-processing step might be needed to further refine the classification process.

5. Discussion
Through the development of this work, some critical aspects should be addressed for further discussion.

5.1 Modelling events at the detector level
It is critical to ensure a return rate with at least one photon reaching the detector. Specifically, when dealing with signal only, we saw that if we rely only on the probability of the signal, we might bias the behaviour of the response, since no signal will be very likely to come from a distribution with a mean rate of zero.

5.2 Improvement of system response
Even though we were able to generate synthetic observations very close to the real ones, further modelling of the noise and of the signal can be done. The latter is not deemed critical for the classification problem by itself, but could become of paramount relevance when assessing the quality of the observables.

5.3 Variability in orbit and system constraints
So far, we have tested one orbit type only, with different system configurations. These tests have to be extended to consider different target types, orbital regimes, system configurations, and system availability. The results are, however, encouraging and the simulation tool was done to ensure that future tests could be done in a very pragmatic and fast fashion.

5.4 Optimization of parameters
We have seen that the detection procedure is sensitive to the type of parameters that are defined in the classification step. In this work, a combination of threshold, size and shape per bin was shown, but further work needs to be conducted to further assess the interdependencies that exist between these parameters. In addition, besides successfully detecting the signal, it is important to derive a figure of merit for the reliability that we have on the data being classified as signal. We should derive a metric based on the assumption of the physical process rather than relying on a subsequent orbit determination procedure, which will just remove the outliers. The reason being, that for very short arcs an orbit improvement might not be even possible.

5.5 Further improvements
So far, we have provided insights into a classification step according to the distribution of OmC residuals vs. epoch registration events. Besides the optimization of parameters involved in the generation of a certain grid
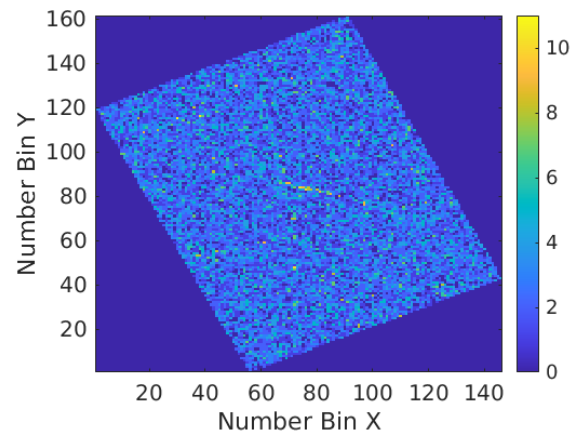
Fig. 11. Resulting bivariate histogram after applying a linear transformation to the data set OmC vs. epoch registration of the even corresponding to the case where the signal-to-noise ratio was compromised.

for the generation of bivariate histograms, there are other ideas to be further developed, which could potentially help in revealing the actual concentration of photons that are reflected by the target object of interest, but due to e.g., a steep signature or even a tumbling motion, is not possible to get. An example of such attempts of applying a linear transformation to the OmC vs. epoch registration event is shown in Fig. 11. There

we can see how the steep signature, which is visible in the right-upper plot in Fig. 6 is flattened after applying a linear transformation to the original data set. The linear transformation will correspond to a tilt on the bins of the original bivariate histogram.

6. Summary
In this work, we presented a comprehensive study aiming at the correct classification of return signals from weak returns of laser ranging observations to non-cooperative objects. We revised the models and assumptions that provided the basis for a simulation tool that is able to generate raw observations according to the technical specifications of a given system and reference orbits and characteristics of a defined target object. The resulting classification step was assessed qualitatively by visual inspection, and quantitatively using ROC curves. To optimize the detection process, we used the ROC curves to find an optimal setup for generating bivariate histograms for the correct discrimination of the signal from the noise.

References

[1] Rodriguez-Villamizar, J., & Schildknecht, T. (2022). Daylight Measurement Acquisition of Defunct Resident Space Objects Combining Active and Passive Electro-Optical Systems. IEEE transactions on geoscience and remote sensing, 60, 1-17.

[2] Steindorfer, M. A., Kirchner, G., Koidl, F., Wang, P., Jilete, B., & Flohrer, T. (2020). Daylight space debris laser ranging. *Nature Communications*, *11*(1), 3735.

[3] Zhang, Z. P., Yang, F. M., Zhang, H. F., Wu, Z. B., Chen, J. P., Li, P., & Meng, W. D. (2012). The use of laser ranging to measure space debris. Research in Astronomy and Astrophysics, 12(2), 212.

[4] Liang, Z., Dong, X., Ibrahim, M., Song, Q., Han, X., Liu, C., & Zhao, G. (2019). Tracking the space debris from the Changchun Observatory. Astrophysics and Space Science, 364, 1-9.

[5] Gibbs, P., Potter, C., Sherwood, R., Wilkinson, M., Benham, D., Smith, V., & Appleby, G. M. (2006). Some early results of kilohertz laser ranging at Herstmonceux. In *Proceedings of 15th international workshop on laser ranging* (pp. 250-258).